AIAA JOURNAL
Vol. 44, No. 12, December 2006

# Low-Velocity Impact Response of Small-Angle Laminated Composites

Adam L. Pilchak,* Takashi Uchiyama,† and Dahsin Liu‡
*Michigan State University, East Lansing, Michigan 48824*

DOI: 10.2514/1.22380

**Reducing delamination is essential in increasing the impact resistance of laminated composites. In this study, two methods were used to improve energy-absorption capabilities of laminated glass/epoxy composites; one was based on small fiber angle changes between adjacent laminae, and the other was based on through-thickness stitching reinforcement. Penetration thresholds were determined for small-angle laminated composites $[0/\theta]_6$ for which $\theta = 0$, 5, 10, and 15 deg. The small-angle laminated composites, especially $[0/15]_6$, were found to have higher penetration thresholds than the conventional large-angle laminated composites, such as $[0/90]_6$, due to damage progression (most notably, fiber bridging). Stitched small-angle laminated composites were also found to have higher impact resistance than unstitched specimens with the same stacking sequence. The use of small-angle composites was extended to multi-axis laminated composites, such as biaxis, triaxis, and sexiaxis laminated composites. Penetration thresholds of the multi-axis laminates were found to be very comparable with the uniaxis laminated composites, that is, $[0/\theta]_6$.**

## I. Introduction

FIBER-REINFORCED polymer matrix composite materials have been used extensively in the aerospace industry, due to their high specific stiffness and high specific strength. Although laminated plates made of composite materials have excellent in-plane properties, they are very susceptible to impact loading. Transverse impact loading can cause delamination at the interfaces between adjacent lamina with dissimilar fiber orientation. Although delamination does not provide significant amounts of energy absorption during the impact of laminated glass/epoxy composites [1], it does cause significant structural disintegration to the composite laminates and makes them vulnerable to subsequent loadings [1].

Several methods have been pursued to reduce delamination in composite laminates, including stitching [2–4], z pinning [4–6], and three-dimensional weaving [7–12]. These techniques are all based on enhancing through-thickness strength by adding additional fibers or pins. They show promising results in applications that require high impact resistance; however, uses in structural applications have been limited, due to the possible reduction of in-plane properties caused by stitching-induced stress concentrations.

A novel three-dimensional woven composite has been developed by Coppens [13]. It has been found to be an effective way to suppress delamination and to improve energy-absorption capabilities of composite materials. This method focuses on designing fiber geometry rather than introducing additional reinforcement in the thickness direction. This technique is based on the manufacturing process of conventional woven fabrics; however, the weaving strands are not restricted to one layer. The fibers interlock with adjacent layers to produce a three-dimensional woven structure in which each layer is integrated with both layers adjacent to it. This is much different from the traditional three-weave composites that are currently available. The commercially available three-weave products are made by stacking several layers of unidirectional fibers, either with the same fiber orientation or with different fiber orientations. The stacked layers are then stitched in the through-thickness direction with additional fibers. There is no undulation in the three-weave fibers as there is with conventional woven fabric and, therefore, the high stiffness and high strength of straight fibers can be retained. It has been reported that stitching fibers with 2% of weight volume is sufficient for resisting delamination in the three-weave composites [8,12].

The damage process of composite laminates subjected to low-velocity impact is very complex. In addition to delamination, other damage modes (such as matrix cracking, fiber breakage, and fiber-matrix debonding) may take place. The role of individual damage modes changes as the stacking sequence of the laminate changes. Liu [14] has suggested that differences in bending stiffness between laminae having different fiber orientation can affect the size of the delamination area. Similarly, Tao and Sun [15] have reported that delamination occurs at interfaces for which there were differences in fiber orientation.

Delamination plays a critical role in impact-induced damage of composite laminates. Delamination is dependent on the stacking sequence and, more importantly, the angle difference between adjacent plies. To improve impact resistance and energy-absorption capabilities of laminated composites, the present study investigates the effect of small-angle changes between adjacent laminae [1,13] as a means of suppressing delamination. The damage mechanisms of small-angle laminated composites are of primary interest. The effect of stitching on impact resistance of small-angle laminated composites is also presented. The use of small-angle composites in general laminated composite designs is explored by investigating biaxis, triaxis, and sexiaxis composites.

## II. Manufacture and Testing

Unidirectional glass/epoxy prepreg (3M type 1003A) was used to construct laminated $300 \times 300$ mm specimens with stacking sequences $[0]_{12}$, $[0/5]_6$, $[0/10]_6$, and $[0/15]_6$. A second set with stacking sequence $[0]_{12}$, $[0/5]_6$, and $[0/10]_6$ was stitched with 1.5-mm-wide strips of prepreg cut parallel to the fiber direction. The specimens with stitching will use the prefix S to differentiate them from the unstitched specimens, which will use the prefix L to describe that they are only laminated, with no additional through-thickness strengthening. The stitching density and pattern was consistent for all stitched specimens (Fig. 1). Each stitching node was 12.7 mm from the adjacent ones and each row was offset 6.35 mm from the one above or below it. The specimens were layered with

Received 10 January 2006; revision received 8 August 2006; accepted for publication 15 September 2006. 

*Student, Chemical Engineering and Materials Science, Engineering Building, Room 2527. Student Member AIAA.
†Visiting Scholar, on Leave from Japan Patent Office, Tokyo, Japan.
‡Professor, Mechanical Engineering, Engineering Building, Room 2555. Member AIAA.

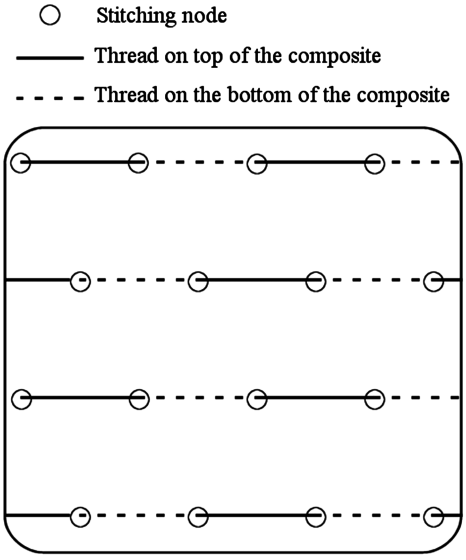


**Fig. 1 Stitching pattern for S[0/$\theta$]$_6$ specimens.**

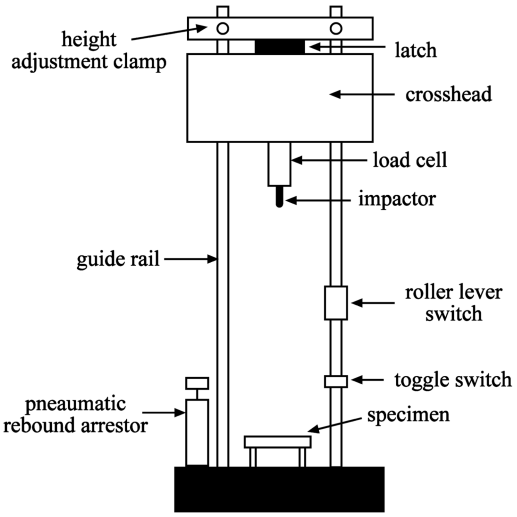


**Fig. 2 Schematic of drop-weight impact testing facility.**

fabrication-related materials, such as release film, resin absorber, mold plates, and vacuum bags. These specimens were cured in an autoclave at 175°C with a heating and cooling rate of 5.5°C/ min. The isothermal hold time was 45 min and the pressure was held at 0.56 MPa during heating, dwelling, and cooling. No vacuum was imposed in the fabrication.

The cured composites were then cut into 100 × 100 mm square specimens with a diamond blade circular saw. The specimens were tested with an instrumented drop-weight tower, shown schematically in Fig. 2. The loading unit consisted of a 22.24 kN load cell, a 50.8-mm-long impactor with a 12.7-mm-diam hemispheric tip, and a crosshead. The impactor had a mass of 92.4 g, whereas the total mass of the loading unit $m$ was 5.03 kg. The impact energy (IE) was controlled by varying the height $h$ between the tip of the impactor and the top surface of the sample, using the height adjustment clamp. The impact energy was determined by $\mathrm{IE} = mgh$, where $g$ is the acceleration due to gravity. The initial impact energies for a given sample were chosen based on the data from previous studies [1,2]. Based on the results of the first test, whether the impactor rebounded or perforated the specimen, the height of the impactor was either raised or lowered. The change in height was estimated by observing the specimen damage and also evaluating the load-displacement curve recorded during the impact event. The specimens were held in place by a system of four toggle clamps to ensure that a fixed clamping pressure was used for each experiment. The specimens were sandwiched between two 2.54-cm-thick steel plates that left 76 × 76 mm of the specimen exposed. The bottom plate was fixed to the base of the testing equipment and the top plate was removable and held in place only by the clamping system. When the crosshead was dropped, it would press a roller switch with its leading edge and maintain contact until just before the impactor contacted the surface. At this time, a toggle switch would be activated by the crosshead, which would turn the circuit on. If the impactor rebounded from the surface of the specimen, the top surface of the crosshead would strike the roller switch, which would activate a solenoid via a relay and extend an air cylinder to push the crosshead upwards. This held the impactor above the surface of the specimen to ensure that all damage was due to only one impact event.

## III. Discussion

### A. Small-Angle Effect

The impact response of composite materials can be broadly divided into three categories: rebounding, penetration, and perforation. When the impactor rebounds, the energy absorbed by the sample is less than the impact energy. As impact energy is increased, the impactor will penetrate into the specimen and not rebound, thus absorbing all of the impact energy. The critical value at which all the impact energy is absorbed by the sample is the so-called penetration threshold. There is a range of impact energies associated with penetration in which the absorbed energy and the impact energies are theoretically equal. However, some of the impact energy can be lost due to vibration of the testing fixture, and so the absorbed energy measured by the load cell is not always exactly equal to the impact energy. The range of equal energy is more easily determined in thicker specimens. After the equal energy interval, the impactor completely penetrates (or perforates) the specimen, and the absorbed energy again becomes less than the impact energy. The perforation threshold is the energy at which the impactor exits the back of the specimen. Coppens [13] and Liu [1] reported an increase in penetration threshold as the fiber orientation mismatch between adjacent laminae decreased, particularly when the mismatch was 15 deg. The triangles ($\Delta$) in Fig. 3 represent the penetration thresholds for laminated glass/epoxy composites from Coppens's study [13]. The results in Fig. 3 indicate a mild increase in impact resistance in unstitched laminated glass/epoxy specimens [0/$\theta$]$_6$ for small values of $\theta$. The highest impact resistance seems to exist between $\theta = 7.5$ and $\theta = 15$. Stitching was performed on a specimen based on the stacking sequence [0/90]$_6$, resulting in S[0/90]$_6$ The filled triangle (▲) in Fig. 3 indicates that the impact resistance of the stitched specimen over the unstitched counterpart is around 4 J. The present study was focused on small angles between adjacent plies of

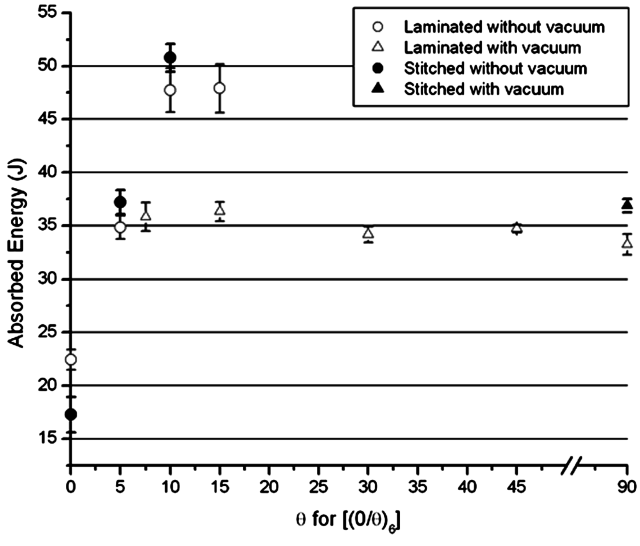


**Fig. 3 Penetration thresholds for [0/$\theta$]$_6$ glass/epoxy composites.**

laminated and stitched composites with $\theta = 0$, 5, 10, and 15 for stacking sequence of $[0/\theta]_6$.

Figure 3 also reports the penetration thresholds of the specimens in the present study. The circles (○) are the laminated specimens and the filled circles (●) are the stitched specimens. It should be noted that the specimens used in Coppens's study were manufactured using an autoclave and by applying pressure and vacuum. The specimens from the present study were cured in the same autoclave with the same pressure but without vacuum, and so they were thicker (average thickness was 3.28 mm and fiber volume fraction was 0.50) than Coppens's specimens (average thickness was 2.6 mm and fiber volume fraction was 0.67). This could account for the dramatic increase in impact resistance for the specimens used in the present study, although they were made from the same material and had the same number of plies.

In the small-angle regime ($\theta \leq 15$), the effect of fiber orientation is very significant. In Fig. 3, the unstitched (i.e., laminated) specimens $L[0/15]_6$ have the highest penetration threshold, followed by $L[0/10]_6$ and then by $L[0/5]_6$. The unidirectional specimens $L[0]_{12}$ have the lowest penetration threshold. This implies that there is an angle near 15 deg that provides the highest impact resistance.

When stitched specimens were investigated, a similar trend in increasing impact resistance with increasing angle was noticed for $S[0/\theta_6]$ specimens in which $\theta$ was between 0 and 10. As $\theta$ increased, the difference in penetration thresholds between laminated and stitched composites of the same stacking sequence also increased. When $\theta = 0$, the stitched specimens had a lower penetration threshold than the laminated counterparts, around 5 J less. The stitched specimens $S[0/5]_6$ exhibited a 2.3-J increase in penetration threshold over the laminated specimens $L[0/5]_6$, whereas $S[0/10]_6$ had a 3.3-J increase over $L[0/10]_6$. No data were available for $S[0/15]_6$ and so a comparison could not be made. The penetration thresholds presented in Fig. 3 are based on performing nine instrumented drop-weight experiments for each type of sample. The penetration thresholds of at least five independent tests were averaged to obtain the penetration threshold for a particular type of sample. The technique to determine the penetration threshold is discussed in the following sections.

### B. Load-Deflection Curves

An investigation of the damage mechanisms is necessary to explain the increase in impact resistance due to the small-angle effect and stitching. This discussion will be based on load-deflection curves and corresponding damaged specimens to identify the dominant damage modes at different stages during an impact event. The load-deflection curves for all nine $L[0/10]_6$ specimens are shown in Fig. 4. They seem to match well on both loading and unloading sections, implying the materials and experiments were very consistent and repeatable. Curves 1, 2, 4, 5, and 6 are closed, meaning the impactor rebounded and did not penetrate the specimens. Curves 3, 7, 8, and 9 are open curves, indicating the specimens were perforated. The impact energy values corresponding to the load-deflection curves in Fig. 4 are presented in Table 1.

**Table 1 Impact energies corresponding with the load-deflection relationship in Fig. 4**

| Sample ID | Impact energy, J | Result |
|---|---|---|
| 1 | 40.1 | Rebound |
| 2 | 41.4 | Rebound |
| 3 | 50.5 | Penetrate |
| 4 | 43.0 | Rebound |
| 5 | 46.4 | Rebound |
| 6 | 51.3 | Rebound |
| 7 | 56.2 | Penetrate |
| 8 | 54.8 | Penetrate |
| 9 | 53.2 | Penetrate |

A representative load-deflection relationship was constructed for $L[0/10]_6$ specimens by averaging the data points for all nine tests. The data points after maximum deflections for those specimens that caused the impactor to rebound were neglected in this average. The averaged curve is shown in Fig. 5, along with the load-deflection curve for specimen 8 that seems to match well with the averaged curve. The discussion of the damage process of $L[0/10]_6$ will be based on specimen 8.

Figure 5 also illustrates some important features of the load-deflection relationship of specimen 8 that were commonly observed during all impact events. When the impactor first contacted the specimen surface (Fig. 6a), it caused indentation and associated matrix damage on the specimen, resulting in the first apparent bump 1, the so-called inertial peak, in the load-deflection curve. As the impactor continued to deflect the specimen, delamination was the next type of damage to occur. This took place at the critical point 2 [16], which corresponds with a critical load and a critical deflection represented by dashed lines. The critical point can be determined by finding the intersection point between two linear regression lines that are fit to the two regions in the load-deflection curve with different slope, as also shown in Fig. 5. Note that the inertial peak was not used in the fit of the first region. The critical load occurred at nearly 1.40 kN, with the corresponding critical deflection around 3.55 mm for specimen 8. The slope of the line before the critical point 3 is $m_1 = 396$ N/mm, whereas that after the critical point $m_2$ is 597 N/mm. They represent the stiffness of the composite before and after the critical point, respectively. The higher stiffness after the critical point was likely due to the in-plane force (i.e., membrane force) caused by the fixed boundaries of the specimens. The onset of

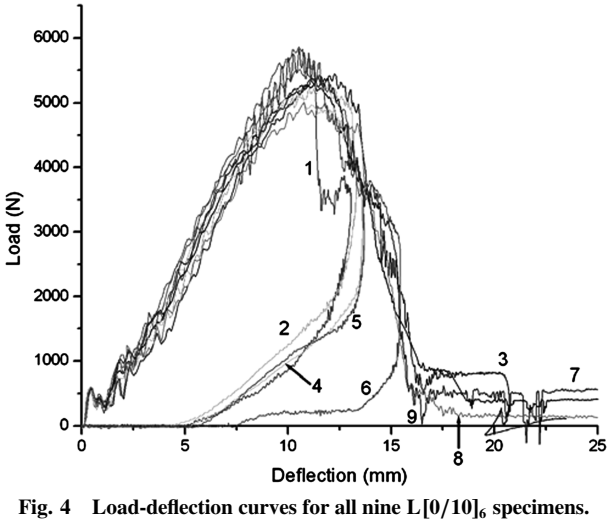


**Fig. 4 Load-deflection curves for all nine $L[0/10]_6$ specimens.**

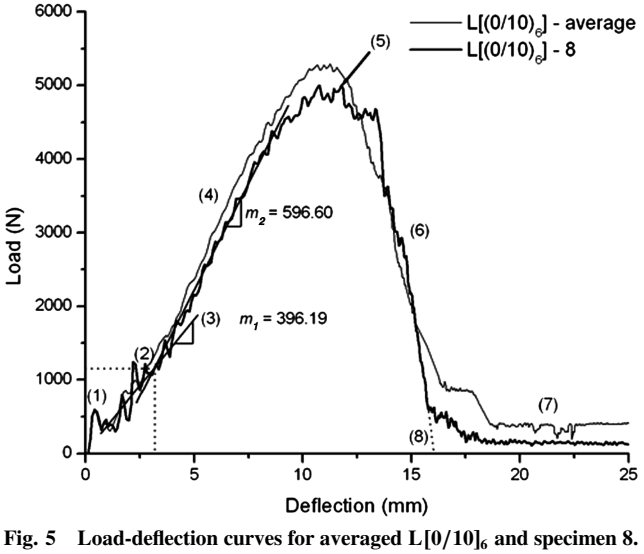


**Fig. 5 Load-deflection curves for averaged $L[0/10]_6$ and specimen 8.**

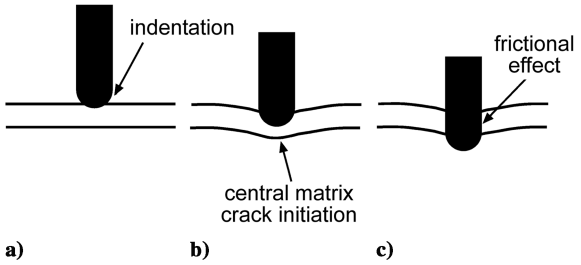


**Fig. 6 Schematic representation of the interaction between the composite specimen with fixed boundary conditions and the impactor: a) in the initial stages of impact, b) during impact, and c) near the end of impact.**

delamination was identified to be around the critical point of (3.55 mm, 1.40 kN).

As the impact load increased, a central matrix crack formed in the postcritical stage 4. The central crack nucleated on the back face of the composite, due to tensile stresses applied during impact (Fig. 6b). The central crack was always aligned parallel to the fiber direction on the back face of the specimen, the 10-deg direction in this case. The central crack did not cause immediate disintegration of the composite. Instead, there was a plateau around the peak force 5 of 5.01 kN. Deviation from the tangential line 4 suggested that the composite was gradually weakened before the plateau around peak force was reached. The reduction in stiffness was primarily caused by the extension of the central crack to the boundary of the specimens, side cracks, also along the 10-deg direction, and matrix cracks in the indentation area (Fig. 7a). The plateau around peak force in the $L[0/10]_6$ specimens was not observed in laminated composites with large angles between adjacent plies and was attributed to more complex microstructural damage processes, including fiber bridging. Fiber bridging is shown schematically in Fig. 7b. The fibers in the 0-deg orientation span the gap created by the matrix crack along the 10-deg direction.

In the unloading section 6 of the load-deflection curve, there is a significant reduction in load after the plateau of peak force. There seems to be a step on this portion of the curve. The central matrix crack has widened and causes some fiber fracture at the center of the composite. Once enough fibers are fractured, the impactor pushes the remaining fibers out of the way, resulting in low energy absorption for this region.

The nonzero load after perforation 7 is due to friction, because the circumference of the impactor continued to contact the specimen during penetration and after perforation until it used its total impact energy (Fig. 6c). To identify the absorbed energy for penetration, it is necessary to remove the frictional effects after penetration. The method used in the present study involves making a linear regression fit of region 6 in Fig. 5 and extending it to the deflection axis 8. The absorbed energy for penetration is the area bounded by the loading section, the unloading section, the extended section and the deflection axis. In cases of rebounding, a linear regression fit to the data points in region 6 before the deflection began to decrease would estimate the impact energy increase required for penetration rather than remove frictional effects. This method is thus appropriate for specimens that had load-deflection curves very close to the perforated ones. For example, this method was applied to specimen 6 in Fig. 3. The actual energy absorbed was about 47.5 J, whereas the estimated absorbed energy for penetration was estimated to be 49.0 J. Averaging the corrected absorbed energies for penetration yielded the penetration threshold for a particular specimen type. For $L[(0/10)_6$, composite specimens samples 3, 6, 7, 8, and 9 were used and had a penetration threshold of $47.5 \pm 2.0$ J. Specimens that only caused rebounding and had considerably lower impact energy (samples 1, 2, 4, and 5) were used to evaluate damage progression due to impact; however, they were not used in calculating the penetration threshold, because the error in estimating the penetration threshold would have been too great.

### C. Fiber Bridging

When $L[(0/10)_6$ specimens were impacted on the 0-deg ply front face, the 10-deg plies suffered central matrix cracks. The 0-deg plies had central fiber-matrix debonding, resulting in the fibers from the 0-deg plies bridging the matrix crack in the 10-deg plies, as shown by the stereo microscope image in Fig. 8. The small-angle specimens had continuous matrix cracks extending from the contact zone to the boundary clamps on both sides of the specimen, as well as visible side cracks. Suppression of delamination due to central matrix cracking would result in fiber bridging. When delamination outperformed central matrix cracking, fiber bridging would not take place.

As mentioned earlier, the plateau around the peak force in $L[(0/10)_6$ specimens was due in part to fiber bridging. This fiber bridging mechanism was only observed in $L[0/\theta]_6$ specimens in which $\theta = 5$, 10, and 15. Fiber bridging was not observed in $L[0/\theta]_6$ specimens for $\theta \geq 30$ in Coppens's study [13]. These specimens did not have a central matrix crack extending from the impact zone, nor did they have side cracks, but significant delamination was observed. On the contrary, the small-angle composites had an insignificant amount of delamination. Fiber bridging was responsible for the high penetration thresholds in the small-angle composites.

Delamination was most likely caused by high interlaminar stress levels that arose from a mismatch in bending stiffness between adjacent lamina, although low matrix strength was also responsible for the damage. Larger fiber angle mismatch implied larger bending stiffness mismatches, which led to high interlaminar stress levels [14]. Reduction in impact resistance for large fiber angle differences can be related to increasing delamination area. The impactor would have little difficulty penetrating the specimen after they were delaminated to individual plies. On the other hand, if a composite had no difference of fiber angle between adjacent plies, such as the unidirectional composite, it would have no delamination. When subjected to impact loading, it would suffer central matrix cracking. Composites with a small difference of fiber angle between adjacent plies would tend to behave like the unidirectional ones. However, the

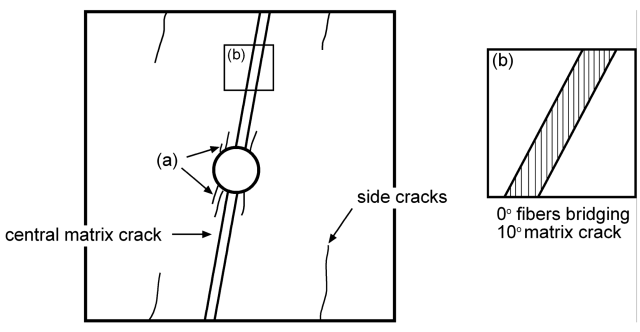


**Fig. 7 Location and damage type in $L[0/10]_6$ specimens; insets show a) matrix cracks in the indentation area of the impactor and b) 0-deg fibers bridging the 10-deg central matrix crack.**

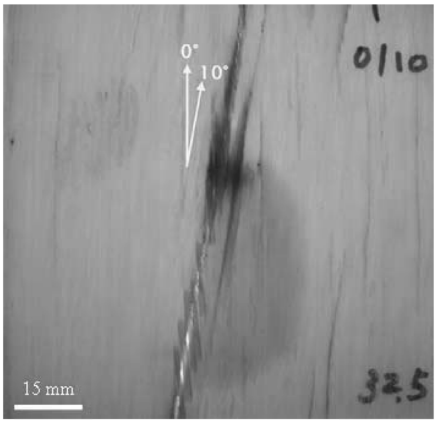


**Fig. 8 Fiber bridging in 0-deg plies in $L[0/10]_6$ specimens.**

**Table 2 Characteristics of small-angle composites**

| Specimen | Impact energy, J | Absorbed energy, J | Critical force, kN | Critical deflection, mm | $m_1$, N/mm | $m_2$, N/mm | Maximum deflection, mm | Peak force, kN |
|---|---|---|---|---|---|---|---|---|
| $L[(0)_{12}]$–9 | 26.0 | 20.8 | - | - | 382 | $m_1 = m_2$ | 12.45 | 2.88 |
| $L[(0/5)_6]$–4 | 36.1 | 34.2 | 0.730 | 2.43 | 386 | 443 | 13.97 | 4.18 |
| $L[(0/10)_6]$–8 | 54.7 | 46.0 | 1.40 | 3.55 | 396 | 597 | 16.22 | 5.00 |
| $L[(0/15)_6]$–2 | 53.5 | 48.6 | 1.99 | 3.52 | 574 | 656 | 14.25 | 6.40 |
| $S[(0)_{12}]$–3 | 25.5 | 19.3 | - | - | 358 | $m_1 = m_2$ | 12.95 | 2.55 |
| $S[(0/5)_6]$–6 | 44.0 | 39.8 | 2.483 | 6.16 | 353 | 596 | 17.54 | 4.43 |
| $S[(0/10)_6]$–7 | 56.4 | 52.8 | 1.629 | 3.90 | 401 | 617 | 16.95 | 5.45 |

small-angle difference at the interfaces would prohibit the central cracks from running through the thickness and result in significant fiber bridging, which was responsible for high energy absorption in the impact process.

### D. Comparison with $L[0]_{12}$, $L[0/5]_6$, and $L[0/15]_6$

The progression of damage for $L[0/10]_6$ could be applied to other laminated specimens with small angles; however, there were some differences. The unidirectional specimens $L[0]_{12}$ had the lowest penetration threshold, due to severe matrix cracking without fiber bridging. The stiffness of unidirectional specimens was 382 N/mm, which was smaller than those of $L[0/5]_6$, $L[0/10]_6$, and $L[0/15]_6$, as shown in Table 2. No significant delamination occurred in these specimens and, consequently, no critical point could be determined. Also, the load-deflection curves did not exhibit a large plateau around peak force and the slope of the unloading section was quite steep, indicating very little resistance in penetration. Figure 9 compares the typical load-deflection curves for each group of laminated specimens; the characteristic values are listed in Table 2 for all specimens in this study.

$L[0/5]_6$ specimens were the first specimens observed to have the fiber bridging strengthening mechanism. The fiber bridges were aligned in the 0-deg direction over the central matrix cracks in the 5-deg direction. The critical point was difficult to locate, due to the similar slopes between $m_1$ and $m_2$; however, examination of these specimens revealed small delamination areas extending along the 5-deg direction. These specimens had a higher stiffness than the unidirectional specimens, which also contributed to the increase in penetration threshold.

$L[0/15]_6$ specimens had an identifiable critical point, 1.99 kN at 3.52 mm (based on $L[0/15]_6$ specimen 2). The slope of the postdelamination region $m_2$ was 656 N/mm, which was the highest of all laminated specimens. These specimens had the highest penetration threshold. This was due to the combined effect of high bending stiffness and fiber bridging. There was, however, a lack of continuous matrix cracking in all of the specimens and no side cracks were developed (Fig. 10). The central matrix cracks in this group of specimens did not cause the specimen to split apart into two separate pieces as was observed in $L[0]_{12}$. These specimens did not almost split apart as in $L[0/5]_6$ and $L[0/10]_6$, in which the central matrix crack spanned the entire composite and the two pieces were only held together by the 0-deg fiber bridges. The catastrophic cracking forced all the fibers in the 0-deg direction to bridge the central matrix crack in $L[0/5]_6$ and $L[0/10]_6$. This was not seen in $L[0/15]_6$; rather, matrix cracks were observed when the specimens were put on a light table. Upon destructive evaluation, the matrix cracks that were oriented in the 15-deg fiber direction were observed to be bridged by the 0-deg fibers. There was also fiber breakage concentrated on the back face beneath the contact-impact zone, which added to the energy absorption.

To obtain the highest penetration threshold, the balance between high bending stiffness and continuous central matrix cracking must be achieved. Both mechanisms seem to contribute during different stages of impact. High bending stiffness causes the load-deflection curve to rise to a high peak force rapidly, whereas continuous matrix cracking promotes a plateau around the peak force, due to fiber bridging. In this study, $L[0/15]_6$ has the highest penetration threshold of all laminated specimens, but it is highly probable that a slightly smaller value for $\theta$ would increase the penetration threshold.

### E. Stitching Effects

Stitching decreased the penetration threshold of $[0_{12}]$ specimens. During the manufacture of stitched specimens, there was localized fiber breakage caused by the stitching needle. These areas became resin-rich during curing and thus became areas of high stress concentration. Matrix cracks tend to nucleate from resin-rich regions. $S[0]_{12}$ specimens had many of these resin-rich inclusions that were introduced by the stitching process and, consequently, failed at lower impact energies, due to the increased amount of the preexisting flaws. Figure 11 shows a comparison of the typical load-deflection relationships for the stitched specimens. The increase in penetration threshold for $S[0/5]_6$ and $S[0/10]_6$ is due to the higher peak force and higher maximum deflection of the stitched specimens, resulting in larger area under the load-deflection curve. This increase can be attributed to bidirectional damage (along both the 0 deg and $\theta$ directions, as shown in Fig. 12) rather than the unidirectional damage

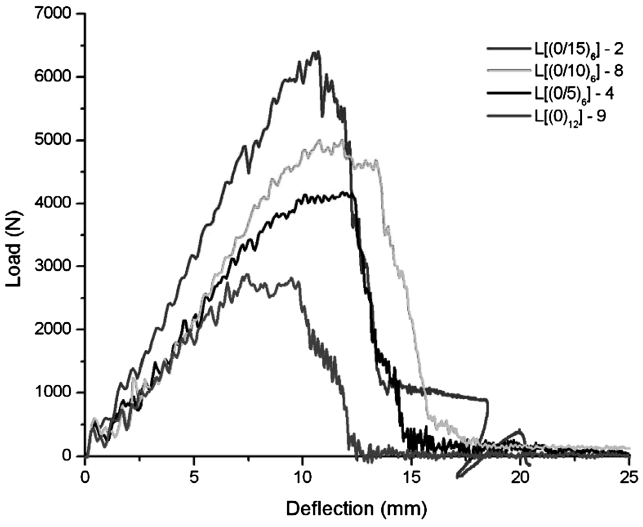


**Fig. 9 Comparison of load-deflection curves for typical laminated specimens.**

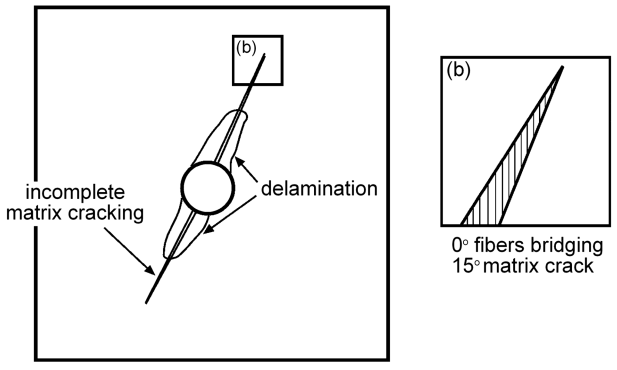


**Fig. 10 Damage progression in $L[0/15]_6$ specimens.**

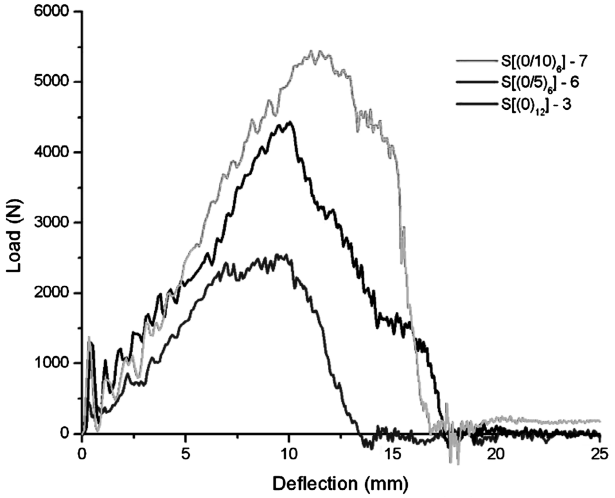


**Fig. 11 Load-deflection curves for typical stitched specimens.**

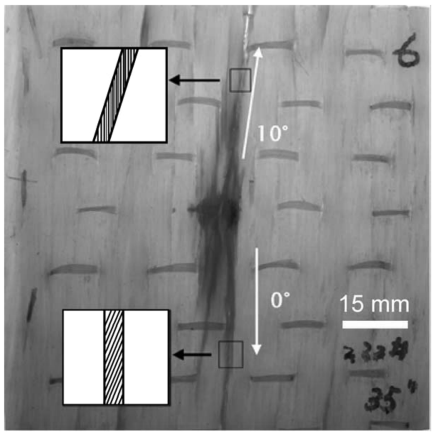


**Fig. 12 Multidirectional damage in S[0/10]$_6$ specimen 6 with schematic cracks and fiber bridges.**

(along the $\theta$ direction only, as shown in Fig. 8) that was observed in the unstitched specimens.

The stitching thread was perpendicular to the 0-deg direction for all specimens, which apparently increased the bending stiffness of the composite laminates. The local fiber breakage around each stitch node assisted the formation of matrix cracks that advanced along the 0-deg direction, which can be seen in Fig. 12. This is not the same as the unstitched specimens that had matrix cracks in the direction of the bottom face, which was the $\theta$ direction. A central matrix crack still existed along the $\theta$ direction with 0-deg fiber bridges; however, a second central matrix crack was observed in the 0-deg direction with 10-deg fiber bridges. The inlays in Fig. 12 show the relative orientation of the types of fiber bridges that formed in L$[0/10]_6$ specimen 6. The unstitched specimens had a plateau around the peak force; this was extended for stitched specimens, due to the bidirectional damage resulting from matrix cracking and fiber bridging in both 0- and 10-deg plies. Furthermore, small cracks advanced from nearly all of the stitching nodes along the 0-deg direction toward the boundaries. The lengths of these cracks ranged from millimeters up to the entire length of the specimen. The stitching nodes nearest the impact point had cracks extending the furthest and the nodes near the boundary clamps had cracks only several millimeters long.

Consistent with observations from the unstitched specimens, samples with higher bending stiffness had higher peak forces. The high peak force combined with larger maximum deflection as a result of bidirectional damage increased the area under the load-deflection curve, although it does not appear to be optimized by these angles. A comparison of the bending stiffness values in Table 2 shows that the bending stiffness was actually increased in some cases. This result is not expected, because stitching typically degrades the in-plane properties of composites. A possible explanation besides stitching could be the difference in impact energies during testing. Variation in impact energy could cause a strain rate effect that resulted in an increase in the bending stiffness of the stitched specimens.

## IV. Multi-Axis Composites for Structural Applications

The inherent anisotropy of the small-angle composites, due to highly oriented fiber direction, limits their use in structural components to applications that experience unidirectional loading. The previous tests were based on small-angle composites: for example, only 0- and 15-deg plies were used and only damage in the 15-deg plies was apparent; hence, they were called uniaxis composite laminates, due to the unidirectional damage. To have more versatile in-plane properties while maintaining high impact resistance, multi-axis laminates were investigated based on the 0/15 unit, which had the highest penetration threshold of the small-angle composites. The use of multiple axes would promote more uniform in-plane damage, rather than concentrated damage along the 15-deg direction, which was observed in the unstitched specimens. Three types of multi-axis composites were fabricated by hot-pressing: 1) biaxis, 2) triaxis, and 3) sexiaxis. A symmetric small-angle composite was also fabricated with a stacking sequence of $[(0/15)_{3s}]$ for comparison. They were all made of the same material as the stitched and unstitched specimens; however, they were cured by a hot press under a pressure of 0.56 MPa at a temperature of 160°C for 45 min. Three biaxis laminates were tested, which had stacking sequences of $[(0/15)_3/(90/-75)_3]$, $[(0/15)_2/(90/-75)_2/(0/15)_2]$, and $[(0/15)/(90/-75)]_3$. Meanwhile, the triaxis and sexiaxis laminates had stacking sequences of $[(0/15)/(60/75)/(-60/-45)]_2$ and $[(0/15)/(30/45)/(60/75)/(90/-75)/(-60/-45)/(-30/-15)]$, respectively. Figure 13 shows the fiber directions for the multi-axis composite laminates.

The multi-axis composite laminates were subjected to low-velocity impact. The three biaxis laminates had a wide range of penetration thresholds, from 44.9 to 54.2 J. Triaxis and sexiaxis composites had penetration thresholds of 49.4 and 50.6 J, respectively. The penetration thresholds are reasonable considering that the symmetric uniaxis laminate $[(0/15)_{3s}]$ absorbed 54.2 J. The characteristics of the multi-axis laminates and the symmetric laminate are shown in Table 3. These results are based on nine tests for each type of specimen. The standard deviation is also reported.

### A. Biaxis Laminates

The biaxis laminates had a damage process similar to the uniaxis composites. At low impact energy, a matrix crack formed along the bottom of the −75-deg ply, followed by a large delamination at the interface between the middle 15- and 90-deg ply in the $[(0/15)_3/(90/-75)_3]$ laminate. The matrix cracks on the top ply were not as well defined as in the $[(0/15)_{3s}]$ laminates. With increasing impact energy, fiber fracture and fiber-matrix debonding occurred at the center of the composite. Fiber fracture occurred on all plies and no continuous matrix cracking along the length of the specimen to the boundary clamps was observed, and so no fiber bridges were formed. The damage on the top ply was slightly larger than for $[(0/15)_{3s}]$, whereas the degree of damage on the bottom ply was significantly larger than in $[(0/15)_{3s}]$ specimens. The fiber-matrix debonding and fiber fracture became so extensive that the composite could no longer support the load of the impactor when perforation occurred.

A more balanced biaxis laminate with a stacking sequence of $[(0/15)_2/(90/-75)_2/(0/15)_2]$ had a slightly different damage process than the $[(0/15)_3/(90/-75)_3]$ laminate. Two extensive delamination zones were observed at the 15/90 interface, as well as at the −75/0 interface. These delamination zones were located one-third of the thickness from the top and bottom surfaces of the composite laminate, whereas a single dominant delamination took place on the midplane of the $[(0/15)_3/(90/-75)_3]$ laminate. The $[(0/15)/(90/-75)]_3$ laminate had more major delaminations at the

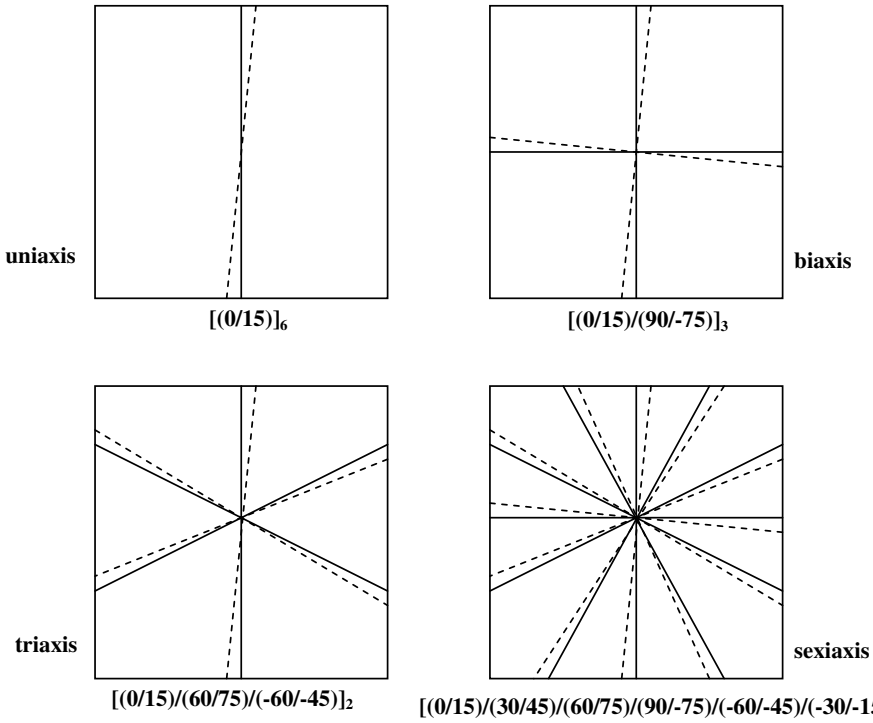


**Fig. 13 Schematic representation of the fiber directions for multi-axis specimens.**

interfaces with a 75-deg difference between adjacent laminae (i.e., 15/90 and −75/0 interfaces). However, the fiber breakage and fiber-matrix debonding in the middle laminae of this composite laminate was not as significant as those in $[(0/15)_3/(90/-75)_3]$ and $[(0/15)_2/(90/-75)_2/(0/15)_2]$.

The variation in impact resistance in biaxis laminates is due to the size and frequency of the delamination zones. The greatest delamination areas occurred at interfaces with the highest fiber orientation mismatch, which was at 15/90 and −75/0 interfaces. There were five of these interfaces in $[(0/15)/(90/-75)]_3$, which had the lowest penetration threshold. The $[(0/15)_3/(90/-75)_3]$ composite had one 75-deg-difference interface on the midplane of the laminate, whereas $[(0/15)_2/(90/-75)_2/(0/15)_2]$ had one 15/90 interface and one 75/0 interface, located at one-third and two-thirds of the thickness. The higher penetration threshold of $[(0/15)_2/(90/-75)_2/(0/15)_2]$, despite having more 75-deg-difference interfaces than $[(0/15)_3/(90/-75)_3]$, was due to the slightly larger damage area, insinuating that more of the specimen contributed to energy absorption.

### B. Triaxis and Sexiaxis Laminates

When loading conditions require more than two-dimensional support, multi-axis laminates (such as triaxis and sexiaxis laminates) can be used. The damage process of $[(0/15)/(60/75)/(-60/-45)_2]$ and $[(0/15)/(30/45)/(60/75)/(-60/-45)/(-30/-15)]$ was very similar to the biaxis laminate $[(0/15)/(90/-75)]_3$, except the direction of the damage changed with the fiber orientation. The degrees of fiber breakage and fiber-matrix debonding were higher than the biaxis laminates in both instances.

The triaxis and sexiaxis laminates absorbed 49.4 and 50.6 J, respectively. This value, although lower than that of the symmetric specimen $[(0/15)_3]_s$ by 4.8 and 3.6 J, respectively, was still a relatively high penetration threshold for laminated glass/epoxy. The high energy absorption was due to the small number of interfaces with large-angle differences. The sexiaxis laminate had 11 15-deg interfaces, whereas the triaxis, which had a lower penetration threshold, had 5 45-deg interfaces and 6 15-deg interfaces.

## V. Conclusions

Small-angle composites with stacking sequences of $[0/\theta]_6$ were shown to have a high penetration threshold compared with a commonly used cross-ply stacking sequence ($[0/90]_6$, for example). The increase was due to a combination of high delamination resistance rising from the small degree of fiber orientation mismatch between adjacent plies and the accompanied fiber bridging mechanism. A central matrix crack formed along the fiber direction on the bottom face of the composite, the $\theta$ direction in this study, with bridges formed by the 0-deg fibers. $L[0/15]_6$ had the highest penetration threshold; however, fiber bridges were not readily observed in all specimens, due to the lack of central matrix cracking. The results seem to suggest that the highest penetration threshold is between 10 and 15 deg. Stitching increased the impact resistance of the laminated glass/epoxy composites. The damage in these composites extended along the 0 deg and $\theta$ directions, which formed matrix cracks and, thus, fiber bridges in both the 0 deg and $\theta$

**Table 3 Average characteristics of multiple-axis laminates**

| Stacking sequence | Absorbed energy, J | Bending stiffness, N/mm | Peak load, kN | No. of interfaces; angle between adjacent plies |
|---|---|---|---|---|
| $[(0/15)_3]_s$ | 54.2 ± 0.9 | 1185 | 6.70 | (10)–15 deg |
| $[(0/15)_3/(90/-75)_3]$ | 52.3 ± 1.0 | 739 | 5.95 | (1)–75 deg, (10)–15 deg |
| $[(0/15)_2/(90/-75)_2/(0/15)_2]$ | 54.2 ± 1.2 | 722 | 6.43 | (2)–75 deg, (9)–15 deg |
| $[(0/15)/(90/-75)]_3$ | 44.9 ± 0.8 | 865 | 6.63 | (5)–75 deg, (6)–15 deg |
| Triaxis | 49.4 ± 0.9 | 1046 | 8.13 | (5)–45 deg, (6)–15 deg |
| Sexiaxis | 50.6 ± 1.3 | 964 | 7.81 | (11)–15 deg |

directions. The use of small-angle composites for structures that require high impact resistance as well as multi-axis loading was discussed. Biaxis, triaxis, and sexiaxis composites were found to have penetration thresholds that were comparable with that of a symmetric uniaxis composite laminate. The multi-axis composites do not have highly oriented fibers, which make them suitable for structures that experience loading in more than one primary direction.

## Acknowledgments

The financial support from the U.S. Army Tank Automotive Research, Development, and Engineering Center (Douglas Templeton and Basavaraju Raju as the project monitors) and the Japan Patent Office is greatly appreciated.

## References

[1] Liu, D., "Characterization of Impact Properties and Damage Process of Glass/Epoxy Composite Laminates," *Journal of Composite Materials*, Vol. 38, No. 16, 2004, pp. 1425–1442.

[2] Liu, D., "Delamination Resistance in Stitched and Unstitched Composite Plates Subjected to Impact Loading," *Journal of Reinforced Plastics and Composites*, Vol. 9, No. 1, 1990, pp. 59–69.

[3] Mouritz, A. P., "Fracture and Tensile Fatigue Properties of Stitched Fiberglass Composites," *Proceedings of the Institution of Mechanical Engineers Part L, Journal of Materials, Design and Applications*, Vol. 218, No. 2, Professional Engineering, London, 2004, pp. 87–93.

[4] Hosur, M. V., Abraham, A., Jeelani, S., and Vaidya, U. K., "Studies on the Influence of Through-the-Thickness Reinforcement on Low-Velocity and High Strain Rate Response of Woven S2-Glass/Vinyl Ester Composites," *Journal of Composite Materials*, Vol. 35, No. 12, 2001, pp. 1111–1133.

[5] Vaidya, U. K., Palazotto, A. N., and Gummadi, L. N. B., "Low Velocity Impact and Compression-After-Impact Response of Z-Pin Reinforced Core Sandwich Composites," *Journal of Engineering Materials and Technology*, Vol. 122, No. 4, 2000, pp. 434–442.

[6] Partridge, I. K., and Cartie, D. D. R., "Delamination Resistant Laminates by Z-fiber® Pinning, Part 1: Manufacture and Fracture Performance," *Composites Part A: Applied Science and Manufacturing*, Vol. 36, No. 1, 2005, pp. 55–64.

[7] Stobbe, D., and Mohemed, M. H., "3D Woven Composites: Cost and Performance Viability in Commercial Applications," *Proceedings of the 48th International SAMPE Symposium 2003*, Society for the Advancement of Materials and Processing Engineering, Covina, CA, 2003, pp. 1372–1382.

[8] Mohamed, M. H., Bogdanovich, S. E., Dickinson, L. C., Singletary, J. N., and Lienhart, R. B., "A New Generation of 3D Woven Fabric Preforms and Composites," *SAMPE Journal*, Vol. 37, No. 3, 2001, pp. 8–17.

[9] Mohamed, M. H., and Zhang, Z., "Method of Forming Variable Cross-Sectional Shaped Three-Dimensional Fabrics," U.S. Patent No. 5085252, filed 4 Feb. 1992.

[10] Dickinson, L. C., and Mohamed, M. H., "Recent Advances in 3D Weaving for Textile Preforming," *Proceedings of the ASME Aerospace Division*, , Vol. 63, American Society of Mechanical Engineers, Fairfield, NJ, 2000, pp. 3–8.

[11] Bogdannovich, A. E., Wigent, D. E., and Whitney, T. J., "Fabrication of 3D Woven Preforms and Composites with Integrated Fiber Optic Sensors," *SAMPE Journal*, Vol. 39, No. 4, 2003, pp. 6–15.

[12] Singletary, J. N., and Bogdanovich, A. E., "Processing and Characterization of Novel 3D Woven Composites," *The 46th International SAMPE Symposium*, Society for the Advancement of Materials and Processing Engineering, Covina, CA, 2001, pp. 835–846.

[13] Coppens, G. J., "Effects of Three-Dimensional Geometry on Penetration and Perforation Resistance," M.S. Thesis, Dept. of Mechanical Engineering, Michigan State Univ., East Lansing, MI, 2004.

[14] Liu, D., "Impact-Induced Delamination: A View of Material Property Mismatching," *Journal of Composite Materials*, Vol. 22, No. 7, 1988, pp. 674–691.

[15] Tao, J., and Sun, C. T., "Influence of Ply Orientation on Delamination in Composite Laminates," *Journal of Composite Materials*, Vol. 32, No. 21, 1998, pp. 1933–1947.

[16] Feraboli, P., and Kedward, K. T., "Enhanced Evaluation of the Low-Velocity Impact Response of Composite Plates," *AIAA Journal*, Vol. 42, No. 10, 2004, pp. 2143–2152.

A. Roy
*Associate Editor*